Theoretical and observational constraints on the H I intensity power spectrum

Hamsa Padmanabhan,[1][*] T. Roy Choudhury[2] and Alexandre Refregier[3]

[1]*Inter-University Centre for Astronomy and Astrophysics, Pune 411007, India*
[2]*National Centre for Radio Astrophysics, Tata Institute of Fundamental Research, Pune 411007, India*
[3]*Institute for Astronomy, Eidgenössische Technische Hochschule Zurich, Wolfgang-Pauli-Strasse 27, CH-8093 Zürich, Switzerland*

ABSTRACT

Mapping of the neutral hydrogen (H I) 21-cm intensity fluctuations across redshifts promises a novel and powerful probe of cosmology. The neutral hydrogen gas mass density $\Omega_{H I}$ and bias parameter $b_{H I}$ are key astrophysical inputs to the H I intensity fluctuation power spectrum. We compile the latest theoretical and observational constraints on $\Omega_{H I}$ and $b_{H I}$ at various redshifts in the post-reionization universe. Constraints are incorporated from galaxy surveys, H I intensity mapping experiments, damped Lyman α system observations, theoretical prescriptions for assigning H I to dark matter haloes and the results of numerical simulations. Using a minimum variance interpolation scheme, we obtain the predicted uncertainties on the H I intensity fluctuation power spectrum across redshifts 0–3.5 for three different confidence scenarios. We provide a convenient tabular form for the interpolated values of $\Omega_{H I}$, $b_{H I}$ and the H I power spectrum amplitude and their uncertainties. We discuss the consequences for the measurement of the power spectrum by current and future intensity mapping experiments.

Key words: cosmology: observations – cosmology: theory – large-scale structure of Universe – radio lines: galaxies.

1 INTRODUCTION

Since the theoretical predictions by Hendrik van der Hulst in 1944 and the first observations by Ewen & Purcell (1951) and Muller & Oort (1951), the 21-cm hyperfine line of hydrogen remains a powerful probe of the H I content of galaxies and now promises to revolutionize observational cosmology. This emission line allows for the measurement of the intensity of fluctuations across frequency ranges or equivalently across cosmic time, thus making it a three-dimensional probe of the universe. It promises to probe a much larger comoving volume than galaxy surveys in the visible band, and consequently may lead to higher precision in the measurement of the matter power spectrum and cosmological parameters. Since the power spectrum extends to the Jeans length of the baryonic material, it allows sensitivity to much smaller scales than probed by the CMB. The inherent weakness of the line transition prevents the saturation of the line, thus enabling it to serve as a direct probe of the neutral gas content of the intergalactic medium during the dark ages and cosmic dawn prior to the epoch of hydrogen reionization.

In the post-reionization epoch ($z \lesssim 6$), the 21-cm line emission is expected to provide a tracer of the underlying dark matter distribution due to the absence of the complicated reionization

astrophysics; hence, it may be used to study the large-scale structure at intermediate redshifts (Bharadwaj & Sethi 2001; Bharadwaj, Nath & Sethi 2001; Bharadwaj & Srikant 2004; Wyithe & Loeb 2008, 2009; Bharadwaj, Sethi & Saini 2009; Wyithe & Brown 2010). H I gas in galaxies and their environments is also a tool to understand the physics of galaxy evolution (Wyithe 2008). At low redshifts $z \sim 1$, these observations are also expected to serve as a useful probe of dark energy (Chang et al. 2010); the acoustic oscillations in the power spectrum may be used to constrain dark energy out to high redshifts $z \gtrsim 3.5$ (Wyithe, Loeb & Geil 2008).

Several surveys, both ongoing and being planned for the future, aim to observe and map the neutral hydrogen content in the local and high-redshift universe. These include the H I Parkes All-Sky Survey (HIPASS; Barnes et al. 2001; Meyer et al. 2004; Zwaan et al. 2005), the H I Jodrell All-Sky Survey (Lang et al. 2003), the Blind Ultra-Deep H I Environmental Survey (Jaffé et al. 2012) which search for H I in galaxy cluster environments with the Westerbork Synthesis Radio Telescope (WSRT),[1] with other surveys using the WSRT presenting complementary measurements of H I content in field galaxies (Rhee et al. 2013). Other current surveys include the Arecibo Fast Legacy ALFA Survey (ALFALFA; Giovanelli et al. 2005; Martin et al. 2010) and the GALEX Arecibo SDSS Survey

---

*E-mail: hamsa@iucaa.ernet.in

[1] http://www.astron.nl/radio-observatory/astronomers/wsrt-astronomers

which measures the H I intensity fluctuations on ~1000 optically selected galaxies (Catinella et al. 2010) over the redshift interval $0.025 < z < 0.05$. The Giant Meterwave Radio Telescope (GMRT; Swarup et al. 1991) may be used to map the 21-cm diffuse background out to $z \sim 0.4$ by signal stacking measurements (Lah et al. 2007, 2009). The Ooty Radio Telescope[2] may also be used to map the H I intensity fluctuation at redshift 3.35 (Saiyad Ali & Bharadwaj 2014). Future experiments, with telescopes under development, include the Murchinson Widefield Array,[3] the Square Kilometre Array (SKA),[4] the Low Frequency Array (LOFAR),[5] the Precision Array to Probe the Epoch of Reionization,[6] the WSRT APERture Tile In Focus survey (Oosterloo, Verheijen & van Cappellen 2010), the Karl G. Jansky Very Large Array,[7] the Meer-Karoo Array Telescope (Jonas 2009) and the Australian SKA Pathfinder (Johnston et al. 2008) Wallaby Survey. Many of these telescopes will map the neutral hydrogen content at higher redshifts, $z \sim 6$–50 as well.

There are also surveys that map the H I 21-cm intensity of the universe at intermediate redshifts without the detection of individual galaxies. A three-dimensional intensity map of 21-cm emission at $z \sim 0.53$–1.12 has been presented in Chang et al. (2010) using the Green Bank Telescope (GBT). The Effelsberg–Bonn survey is an all-sky survey having covered 8000 deg^2 out to redshift 0.07 (Kerp et al. 2011). Several intensity mapping experiments over redshifts $z \sim 0.5$–2.5, including the Baryon Acoustic Oscillation Broadband and Broad-beam (BAOBAB; Pober et al. 2013), BAORadio (Ansari et al. 2012), BAO from Integrated Neutral Gas Observations (Battye et al. 2012), CHIME[8] and TianLai (Chen 2012) are being planned for the future. At high redshifts, $z \sim 1.5$–5, the current major observational probes of the neutral hydrogen content have been damped Lyman alpha absorption systems (DLAs). The latest surveys of DLAs include those from the *HST* and the SDSS (Rao, Turnshek & Nestor 2006; Noterdaeme et al. 2009, 2012; Prochaska & Wolfe 2009) and the ESO/UVES (Zafar et al. 2013) which trace the H I content in and around galaxies in the spectra of high-redshift background quasars. The bias parameter for DLAs has been recently measured in the Baryon Oscillation Spectroscopic Survey (BOSS) by estimating their cross-correlation with the Lyman α forest (Font-Ribera et al. 2012) and leads to the computation of the DLA bias at redshift 2.3.

On the theoretical front, cosmological hydrodynamical simulations have been used to investigate the neutral hydrogen content of the post-reionization universe (Duffy et al. 2012; Davé et al. 2013; Rahmati et al. 2013) using detailed modelling of self-shielding, galactic outflows and radiative transfer. The simulations have been found to produce results that match the observed neutral hydrogen fractions and column densities for physically motivated models of star formation and outflows. Analytical prescriptions for assigning H I to haloes have also been used to model the bias parameter of H I-selected galaxies (Marín et al. 2010) and used in conjunction with dark-matter-only simulations (Bagla, Khandai & Datta 2010; Gong et al. 2011; Khandai et al. 2011; Guha Sarkar et al. 2012) and with smoothed particle hydrodynamics (SPH) simulations (Villaescusa-Navarro et al. 2014).

[2] http://rac.ncra.tifr.res.in
[3] http://www.mwatelescope.org
[4] https://www.skatelescope.org
[5] http://www.lofar.org
[6] http://eor.berkeley.edu
[7] https://science.nrao.edu/facilities/vla
[8] http://chime.phas.ubc.ca

It is important to be able to quantify and estimate the uncertainty in the various parameters that characterize the intensity fluctuation power spectrum, for the planning of current and future H I intensity mapping experiments. In this paper, we combine the presently available constraints on the neutral hydrogen gas mass density, $\Omega_{H I}$ and bias parameter, $b_{H I}$ to predict the subsequent uncertainty on the power spectrum of the 21-cm intensity fluctuations at various redshifts. The constraints are incorporated from galaxy surveys, H I intensity mapping experiments, the DLA observations, theoretical prescriptions for assigning H I to dark matter haloes, and the results of numerical simulations. We find that it might be possible to improve upon the commonly used assumption of constant values of $\Omega_{H I}$ and $b_{H I}$ across redshifts by taking into consideration the fuller picture implied by the current constraints. We use a minimum variance interpolation scheme to obtain the uncertainties in $\Omega_{H I}$ and $b_{H I}$ across redshifts from 0 to ~3.5. We consider three different confidence scenarios for incorporating observational data and theoretical predictions. We discuss the resulting uncertainty in the H I power spectrum and the consequences for its measurement by current and future intensity mapping experiments. We also provide a tabular representation of the uncertainties in $\Omega_{H I}$, $b_{H I}$ and the power spectrum across redshifts, implied by the combination of the current constraints.

This paper is organized as follows. In Section 2, we describe in brief the theoretical formalism leading to the 21-cm intensity fluctuation power spectrum and the ingredients that introduce sources of uncertainty. In Section 3, we summarize the current constraints for the parameters in the power spectrum from the observational, theoretical and simulation results that are presently available. In Section 4, we combine these constraints to obtain the uncertainty on the product $\Omega_{H I}b_{H I}$ which directly relates to the uncertainty in the power spectrum discussed in Section 5. We summarize our findings and discuss future prospects in the final concluding section.

2 FORMALISM

2.1 H I intensity mapping experiments

In the studies of 21-cm intensity mapping, the main observable is the three-dimensional power spectrum of the intensity fluctuation, $[\delta T_{H I}(k, z)]^2$, given by the expression (e.g. Battye et al. 2012):

$$[\delta T_{H I}(k, z)]^2 = \bar{T}(z)^2 [b_{H I}(k, z)]^2 \frac{k^3 P_{cdm}(k, z)}{2\pi^2}, \qquad (1)$$

where the mean brightness temperature is given by

$$\bar{T}(z) = \frac{3h_{Pl}c^3 A_{10}}{32\pi k_B m_p^2 \nu_{21}^2} \frac{(1+z)^2}{H(z)} \Omega_{H I}(z)\rho_{c,0}$$

$$\simeq 44\,\mu K \left(\frac{\Omega_{H I}(z)h}{2.45 \times 10^{-4}} \right) \frac{(1+z)^2}{E(z)}, \qquad (2)$$

where $E(z) = H(z)/H_0$, $b_{H I}(k, z)$ is the H I bias, $\rho_{c,0}$ is the critical density at the present epoch ($z = 0$) and $P_{cdm}(k, z)$ is the dark matter power spectrum, A_{10} is the Einstein-A coefficient for the spontaneous emission between the lower (0) and upper (1) levels of hyperfine splitting, ν_{21} is the frequency corresponding to the 21-cm emission and other symbols have their usual meanings. The above expression is calculated by assuming that the line profile, dν, is very narrow and absorption is neglected (which is a valid approximation if the spin temperature of the gas is far greater than the background CMB temperature). Also, it is assumed that the line

width $d\nu/(1 + z)$ is much smaller than the frequency interval of the observation.[9]

As can be seen, the two key inputs to the power spectrum are the neutral hydrogen density parameter, $\Omega_{H I}(z)$ and the bias parameter of H I, $b_{H I}(k, z)$. These represent fundamental quantities in the observations of the H I intensity. In what follows, we will neglect the scale dependence of bias and treat it as a function of the redshift z alone, i.e. $b_{H I}(z)$. This is a valid approximation on large scales where we study the effects on the power spectrum.

2.2 Halo model: analytical calculation of $b_{H I}$ and $\Omega_{H I}$

Here, we briefly outline the analytical formulation using the halo model for the distribution of dark matter haloes, which we use to compute the two quantities $\Omega_{H I}$ and $b_{H I}$. The Sheth–Tormen prescription (Sheth & Tormen 2002) for the halo mass function, $dn(M, z)/dz$, is used for modelling the distribution of dark matter haloes. The dark matter halo bias $b(M)$ is then given following Scoccimarro et al. (2001).

Given a prescription for populating the haloes with H I, i.e. $M_{H I}(M)$, defined as the mass of H I contained in a halo of mass M, we can compute the comoving neutral hydrogen density, $\rho_{H I}(z)$, as

$$\rho_{H I}(z) = \int_{M_{min}}^{\infty} dM \frac{dn(M, z)}{dM} M_{H I}(M) , \tag{3}$$

and the bias parameter of neutral hydrogen, $b_{H I}(z)$ as

$$b_{H I}(z) = \frac{1}{\rho_{H I}(z)} \int_{M_{min}}^{\infty} dM \frac{dn(M, z)}{dM} b(M) M_{H I}(M) . \tag{4}$$

We consider only the linear bias in this paper.

Finally, the neutral hydrogen fraction is computed as (following common convention)

$$\Omega_{H I}(z) = \frac{\rho_{H I}(z)}{\rho_{c,0}} \tag{5}$$

where $\rho_{c,0} \equiv 3H_0^2/8\pi G$ is the critical density at redshift 0.

In the above analytical calculation, we see that the key input is $M_{H I}(M)$, the prescription for assigning H I to the dark matter haloes. This is done in several ways in the literature and the various resulting prescriptions are discussed below and compiled in the lower section of Table 1. These prescriptions have been found to be a good match to observational results. We also consider the distribution of H I in haloes resulting from smoothed particle hydrodynamical simulations (Davé et al. 2013).

Given the values of $\Omega_{H I}$ and $b_{H I}$, the H I power spectrum may be computed following equation (1). We do this using the linear matter power spectrum and the growth function obtained by solving its differential equation (Wang & Steinhardt 1998; Linder & Jenkins 2003; Komatsu et al. 2009). The cosmological parameters assumed here are $\Omega_\Lambda = 0.723$, $h = 0.702$, $\Omega_m = 0.277$, $Y_p = 0.24$, $n_s = 0.962$, $\Omega_b h^2 = 0.023$ which are in roughly good agreement with most available observations including the latest *Planck* results (Planck Collaboration XVI 2014). The primordial power spectrum corresponds to the normalization $\sigma_8 = 0.815$. The matter transfer function is obtained from the fitting formula of Eisenstein & Hu (1998) including the effect of baryonic acoustic oscillations.

---

[9] We do not take into account peculiar velocity-related effects in the present study.

2.3 Damped Lyman alpha systems

In studies measuring the neutral hydrogen fraction using DLAs, the key observables are the sum $\Sigma N_{H I}$ of the measurements of the column density of H I over a redshift interval having an absorption path length ΔX, defined following Lanzetta et al. (1991). From this, the gas density parameter Ω_g^{DLA} is evaluated as

$$\Omega_g^{DLA} = \frac{\mu m_H H_0}{c \rho_{c,0}} \frac{\Sigma N_{H I}}{\Delta X} \tag{6}$$

which is the discrete-N limit of the exact integral expression:

$$\Omega_g^{DLA} = \frac{\mu m_H H_0}{c \rho_{c,0}} \int_{N_{H I,min}}^{\infty} N_{H I} f_{H I}(N_{H I}, X) dN_{H I} dX , \tag{7}$$

where the lower limit of the integral is set by the column density threshold for DLAs, i.e. $N_{H I,min} = 10^{20.3}$ cm^{-2}. In case the sub-DLAs too are accounted for while calculating the gas density parameter, the same limit is usually taken to be 10^{19} cm^{-2} (Zafar et al. 2013). The low-column-density systems, e.g. the Lyman α forest make negligible contribution to the total gas density. In the above expression, μ is the mean molecular weight, m_H is the mass of the hydrogen atom and $\rho_{c,0}$ is the critical mass density of the universe at redshift 0. Also, $f_{H I}(N, X)$ is the distribution function of the DLAs, defined through

$$d^2\mathcal{N} = f_{H I}(N_{H I}, X) dN dX \tag{8}$$

with $\mathcal{N}$ being the incidence rate of DLAs in the absorption interval dX and the column density range $dN_{H I}$. Once Ω_g^{DLA} is known at several redshifts, it is possible to compute the hydrogen neutral gas mass density parameter $\Omega_{H I}^{DLA}$ for an assumed helium fraction by mass. This represents the neutral hydrogen fraction from DLAs alone. The bias parameter b_{DLA} for DLAs may be obtained from cross-correlation studies (Font-Ribera et al. 2012) with the Lyman α forest.

Thus, the two parameters $\Omega_{H I}$ and b_{DLA} may be estimated from DLA observations. However, as we see above, the techniques for the analysis of the DLA observations are different from those used in the galaxy surveys and H I intensity mapping experiments, both in terms of the fundamental quantities and the methods of calculation of $\Omega_{H I}$ and b_{DLA}. It was recently shown, using a combination of SPH simulations and analytical prescriptions for assigning H I to haloes, that it is possible to model the 21 cm signal which is consistent with observed measurements of $\Omega_{H I}$ and b_{DLA} (Villaescusa-Navarro et al. 2014).

3 CURRENT CONSTRAINTS

Table 1 lists the presently available observational and theoretical constraints on the various quantities related to the computation of the H I three-dimensional power spectrum at different redshifts. The details of the various constraints are briefly described in the following.

3.1 Observational

The top half of Table 1 summarizes the current observational constraints, which are briefly described below.

(i) Galaxy surveys:
The ALFALFA surveys 21-cm emission lines from a region of 7000 deg^2, producing deep maps of the H I distribution in the local universe out to redshift $z \sim 0.06$. Martin et al. (2010) use a sample of 10 119 H I-selected galaxies from the $\alpha.40$ survey to calculate

Table 1. Presently available constraints on the various quantities required for calculation of the H I 3D power spectrum at different redshifts. Constraints are broadly grouped into observational and theoretical/simulation. Observational constraints include those from galaxy surveys, DLA observations and H I intensity mapping experiments. The columns list the technique, parameter(s) constrained, the mean redshift/redshift range, where available, and the reference in the literature for each.

Technique	Constraints	Mean redshift (Redshift range)	Reference
Observational			
Galaxy surveys			
ALFALFA 21-cm emission	$\Omega_{\rm H\,I}^a = 3.0 \pm 0.2$	0.026	Martin et al. (2010)
HIPASS 21-cm emission	$\Omega_{\rm H\,I} = 2.6 \pm 0.3$	0.015	Zwaan et al. (2005)
HIPASS, Parkes; H I stacking	$\Omega_{\rm H\,I} = 2.82^{+0.30}_{-0.59}$	0.028 (0–0.04)	
	$\Omega_{\rm H\,I} = 3.19^{+0.43}_{-0.59}$	0.096 (0.04–0.13)	Delhaize et al. (2013)
AUDS (preliminary)	$\Omega_{\rm H\,I} = 3.4 \pm 1.1$	0.125 (0.07–0.15)	Freudling et al. (2011)
GMRT 21-cm emission stacking	$\Omega_{\rm H\,I} = 4.9 \pm 2.2$	0.24	Lah et al. (2007)
H I distribution maps from M31, M33 and LMC	$\Omega_{\rm H\,I} = 3.83 \pm 0.64$	0.0	Braun (2012)
ALFALFA α.40 sample, Millennium simulation	$b_{\rm H\,I} = 0.7 \pm 0.1$ (large scales)	$\sim$0	Martin et al. (2012)
DLA observations			
DLA measurements from *HST* and SDSS	$\Omega_{\rm H\,I} = 5.2 \pm 1.9$	0.609 (0.11–0.90)	
	$\Omega_{\rm H\,I} = 5.1 \pm 1.5$	1.219 (0.90–1.65)	Rao et al. (2006)
	$\Omega_{\rm H\,I} = 4.29^{+0.24}_{-0.23}$	(2.2–5.5)	Prochaska & Wolfe (2009)
	$\Omega_{\rm H\,I}(z)$	(2.0–5.19)	Noterdaeme et al. (2009, 2012)
Cross-correlation of DLA and Lyα forest observations	$b_{\rm DLA} = 2.17 \pm 0.2$	$\sim$2.3	Font-Ribera et al. (2012)
Observations of DLAs with *HST*/COS	$\Omega_{\rm H\,I} = 9.8^{+9.1}_{-4.9}$	<0.35	Meiring et al. (2011)
DLAs and sub-DLAs with VLT/UVES	$\Omega_{\rm H\,I}(z)$	1.5–5.0	Zafar et al. (2013)
H I intensity mapping			
WSRT H I 21-cm emission, $z = 0.1$ and 0.2	$\Omega_{\rm H\,I} = 2.31 \pm 0.4$	0.1	
	$\Omega_{\rm H\,I} = 2.38 \pm 0.6$	0.2	Rhee et al. (2013)
Cross-correlation of DEEP2 galaxy-H I fields at $z = 0.8$	$\Omega_{\rm H\,I}b_{\rm H\,I}r^b = (5.5 \pm 1.5)h$	0.8	Chang et al. (2010)
21 cm intensity fluctuation cross-correlation with WiggleZ survey	$\Omega_{\rm H\,I}b_{\rm H\,I}r = (4.3 \pm 1.1)h$	0.8	Masui et al. (2013)
Auto-power spectrum of H I intensity field combined with cross-correlation with WiggleZ survey	$\Omega_{\rm H\,I}b_{\rm H\,I} = 6.2^{+2.3}_{-1.5}h$	0.8	Switzer et al. (2013)
Theory/Simulation			
SPH simulation using GADGET-2	$M_{\rm H\,I}/M_{\rm halo}$, $M_*/M_{\rm halo}$, $\Omega_{\rm H\,I}(z)$	$\sim$0	Davé et al. (2013)
Hydrodynamical simulation using GADGET-2/OWLs	$\Omega_{\rm H\,I} = (1.4 \pm 0.18)h$	0	
	$\Omega_{\rm H\,I} = (2.5 \pm 0.14)h$	1	Duffy et al. (2012)
	$\Omega_{\rm H\,I} = (3.8 \pm 0.08)h$	2	
N-body simulation, H I prescription	$b_{\rm H\,I}(k, z)$	$\sim$1.5–4 $\sim$1.3, 3.4 and 5.1	Guha Sarkar et al. (2012), Bagla et al. (2010)
N-body simulation, H I prescription combined with Chang et al. (2010)	$\Omega_{\rm H\,I} = (11.2 \pm 3.0)h$ $b_{\rm H\,I} = 0.55 - 0.65$	$\sim$0.8	Khandai et al. (2011)
Non-linear fit to the simulations of Obreschkow et al. (2009)	$M_{\rm H\,I}/M_{\rm halo}, M_*/M_{\rm halo}$	1, 2, 3	Gong et al. (2011)
H I prescription incorporating observational constraints	$b_{\rm H\,I}(z)$	0.0–3.0	Marín et al. (2010)

Note. ^{a}The units of $\Omega_{\rm H\,I}$ are $h^{-1} \times 10^{-4}$. ^{b}Here, r denotes the stochasticity.

the H I mass function (HIMF) and find the cosmic neutral H I gas density $\Omega_{\rm H\,I}$ at $z = 0$. In Martin et al. (2012), the correlation function of H I-selected galaxies in the local universe measured by the α.40 survey, together with the correlation function of dark matter haloes as obtained from the Millennium simulation (Springel et al. 2005), is used to estimate the bias parameter $b_{\rm H\,I}$ in the local universe.

Zwaan et al. (2005) present results of the measurement of the HIMF from the 21-cm emission-line detections of the HIPASS

catalogue whose survey measured the HIMF and the neutral hydrogen fraction from 4315 detections of 21-cm line emission in a sample of H I-selected galaxies in the local universe. This measurement is further used to estimate the neutral hydrogen mass density $\Omega_{\mathrm{H_I}}$ in the local universe.

Lah et al. (2007) present 21-cm H I emission-line measurements using co-added observations from the GMRT at redshift $z = 0.24$. This allows the estimation of the cosmic neutral gas density which can be converted into an estimate for $\Omega_{\mathrm{H_I}}$ at this redshift.

Braun (2012) uses high-resolution maps of the H I distribution in M31, M33 and the Large Magellanic Cloud (LMC), with a correction to the column density based on opacity, to constrain the neutral hydrogen gas mass density at $z = 0$.

Delhaize et al. (2013) use the HIPASS and the Parkes observations of the South Galactic Pole (SGP) field to place constraints on $\Omega_{\mathrm{H_I}}$ at two redshift intervals, (0–0.04) and (0.04–0.13).

Rhee et al. (2013) use the H I 21-cm emission-line measurements of field galaxies with the WSRT at redshifts of 0.1 (59 galaxies) and 0.2 (96 galaxies) to measure the neutral hydrogen gas density at these redshifts.

Freudling et al. (2011) use a set of precursor observations of 18 21-cm emission lines at redshifts between redshifts 0.07 and 0.15 from the ALFA Ultra Deep Survey (AUDS) to derive the H I density $\rho_{\mathrm{H_I}}$ at the median redshift 0.125.

(ii) DLA observations:

Rao et al. (2006) use the *HST* and SDSS measurements of DLAs at redshift intervals 0.11–0.90 (median redshift 0.609) and 0.90–1.65 (median redshift 1.219) to constrain the value of $\Omega_{\mathrm{H_I}}$ at these epochs.

Prochaska & Wolfe (2009) use a sample of 738 DLAs from SDSS-DR5, at redshifts 2.2–5.5, in six redshift bins to constrain the neutral hydrogen gas mass density. Noterdaeme et al. (2009) use 937 DLA systems from SDSS-II DR7 in four redshift bins from 2.15 to 5.2, Noterdaeme et al. (2012) measure $\Omega_{\mathrm{H_I}}^{\mathrm{DLA}}(z)$ using a sample of 6839 DLA systems from the BOSS which is part of the SDSS DR9, in five redshift bins between redshifts 2.0 and 3.5.

Meiring et al. (2011) present the first observations from *HST*/Cosmic Origins Spectrograph (COS) of three DLAs and four sub-DLAs to measure the neutral gas density at $z < 0.35$.

Font-Ribera et al. (2012) use the cross-correlation of DLAs and the Lyman α forest to constrain the bias parameter of DLAs, b_{DLA} at redshift $z \sim 2.3$.

Zafar et al. (2013) use the observations of DLAs and sub-DLAs from 122 quasar spectra using the European Southern Observatory (ESO) Very Large Telescope/Ultraviolet Visual Echelle Spectrograph (VLT/UVES), in conjunction with other sub-DLA samples from the literature, to place constraints on the neutral hydrogen gas mass density at $1.5 < z < 5$. One of the crucial differences between this work and others, e.g. Noterdaeme et al. (2012), is that it accounts for sub-DLAs while calculating the total gas mass.

(iii) H I intensity mapping experiments:

Chang et al. (2010) used the GBT to record radio spectra across two of the DEEP2 optical redshift survey fields and present a three-dimensional 21-cm intensity field at redshifts 0.53–1.12. The cross-correlation technique is used to infer the value of $\Omega_{\mathrm{H_I}} b_{\mathrm{H_I}} r$ (where r is the stochasticity) at redshift $z = 0.8$.

In Masui et al. (2013), the cross-correlation of the 21-cm intensity fluctuation with the WiggleZ survey is used to constrain $\Omega_{\mathrm{H_I}} b_{\mathrm{H_I}} r$.

In Switzer et al. (2013), the auto-power spectrum of the 21-cm intensity fluctuations is combined with the above cross-power treatment to constrain the product $\Omega_{\mathrm{H_I}} b_{\mathrm{H_I}}$ at $z \sim 0.8$.

3.2 Theoretical

The theoretical constraints arise from various prescriptions for assigning H I to dark matter haloes. These prescriptions, for different redshifts, are briefly summarized below.

(i) Redshift $=0$: in Davé et al. (2013), fig. 10 is plotted $M_{\mathrm{H_I}}(M)$ at $z = 0$ from their smoothed particle hydrodynamical simulation. We interpolate the values of $M_{\mathrm{H_I}}(M)$ to obtain a smooth curve.

(ii) Redshift ~ 0: the prescription in Marín et al. (2010) uses a fit to the observations of Zwaan et al. (2005) and gives $M_{\mathrm{H_I}}$ as a function of M at redshift $z \sim 0$.

(iii) Redshifts $z > 0$: the prescription given by Bagla et al. (2010) assigns a constant ratio of H I mass to halo mass at each redshift, denoted by f_1. The constant f_1 depends on the redshift under consideration. For each of the three redshifts considered, $z = 1.5$, 3.4 and 5.1, the value of f_1 is fixed by setting the neutral hydrogen density $\Omega_{\mathrm{H_I}}$ to 10^{-3} in the simulations. The maximum and minimum masses of haloes containing H I gas are also redshift dependent. It is assumed that haloes with masses corresponding virial velocities of less than $30\,\mathrm{km\,s^{-1}}$ and greater than $200\,\mathrm{km\,s^{-1}}$ are unable to host H I. Guha Sarkar et al. (2012) use the above prescription with the results of their *N*-body simulation to provide a cubic polynomial fit to the $b_{\mathrm{H_I}}(k)$ at different redshifts.

A prescription for assigning H I to dark matter haloes at redshift ~ 1, for three different theoretical models has been presented in Khandai et al. (2011), for consistency with the observational constraints of $\Omega_{\mathrm{H_I}}$ at $z \sim 0.8$ (Chang et al. 2010). This is used with an *N*-body simulation to predict, in conjunction with the results of Chang et al. (2010), the neutral hydrogen density $\Omega_{\mathrm{H_I}}$ and the bias factor $b_{\mathrm{H_I}}$ at this redshift.

Gong et al. (2011) provide non-linear fitting functions for assigning H I to dark matter haloes at redshifts $z \sim 1$, 2 and 3, based on the results of the simulations generated by Obreschkow et al. (2009).

Duffy et al. (2012) use results of high-resolution cosmological hydrodynamical simulations with the GADGET-2/OWLS including the modelling of feedback from supernovae, AGNs and a self-shielding correction in moderate density regions, in order to predict $\Omega_{\mathrm{H_I}}$ at $z = 0$, 1 and 2.

The above prescriptions, where analytical forms are available, are plotted in Fig. 1. These functions are subsequently used to generate the bias and neutral hydrogen densities at the corresponding redshifts, $b_{\mathrm{H_I}}$ and $\Omega_{\mathrm{H_I}}$ as described in Section 2.

4 COMBINED UNCERTAINTY ON $\Omega_{\mathrm{H_I}}$ AND $b_{\mathrm{H_I}}$

In this section, we compile the current constraints to formulate the combined uncertainty on the quantities $\Omega_{\mathrm{H_I}}$ and $b_{\mathrm{H_I}}$.

Fig. 2 shows the compiled set of values of the neutral hydrogen density parameter, $\Omega_{\mathrm{H_I}}$ from the observations and theory in Table 1. The theoretical points are obtained by using equation (5) of the formalism described in Section 2.2 using the $M_{\mathrm{H_I}}(M)$ prescriptions described in Section 3.[10] The observational points are shown in colour and the theoretical points are plotted in black.

In Fig. 3 are plotted the analytical estimates for the bias, $b_{\mathrm{H_I}}$ obtained by using equation (4) of the analytical formulation described

---

[10] We set $M_{\min} = 10^9\,h^{-1}\,\mathrm{M_{\odot}}$ and $M_{\max} = 10^{13}\,h^{-1}\,\mathrm{M_{\odot}}$ in all the computations except for those corresponding to the prescription of Bagla et al. (2010) where the explicit values of $M_{\min}$ and $M_{\max}$ are specified for each redshift.
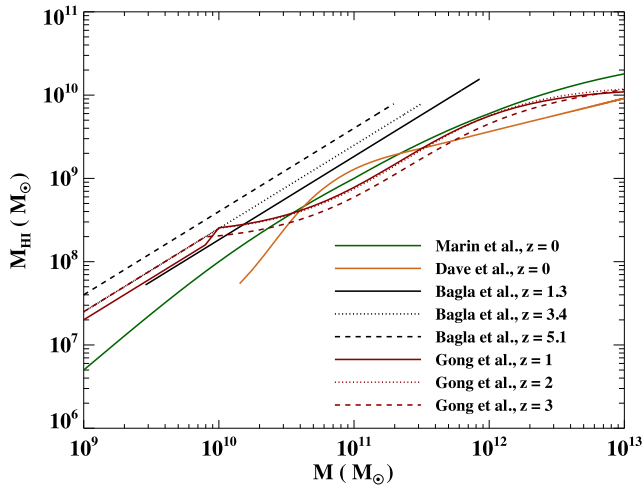
Figure 1. Prescriptions from the literature for assigning H I to dark matter haloes. Results from Davé et al. (2013), Marín et al. (2010) at redshift ∼0, Bagla et al. (2010) at redshifts 1.3, 3.4 and 5.1 and Gong et al. (2011) at redshifts 1, 2 and 3 give M_{HI} as a function of the halo mass M.

in Section 2.2, together with the available prescriptions at the corresponding redshifts. These include (a) the theoretical/simulation prescriptions of Bagla et al. (2010), Marín et al. (2010), Davé et al. (2013), Gong et al. (2011) and the fitting formula of Guha Sarkar et al. (2012) and (b) the measurements of the bias at $z \sim 0$ by the ALFALFA survey (Martin et al. 2012), the combined constraints in
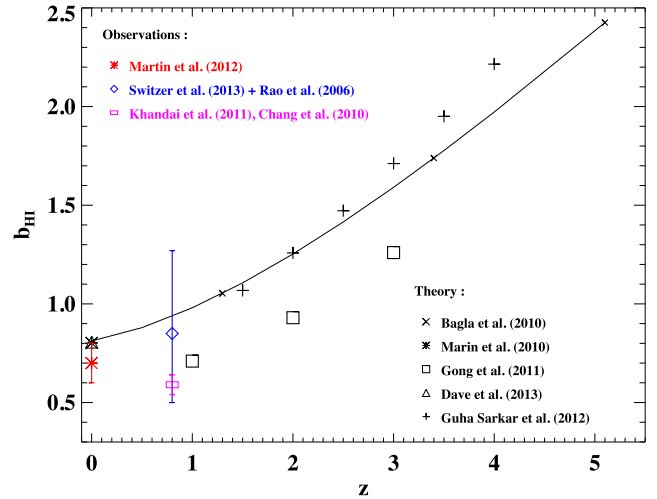

Figure 3. The bias b_{HI} obtained from the theoretical/simulation prescriptions of Bagla et al. (2010), Marín et al. (2010), Davé et al. (2013), Gong et al. (2011) and the fitting formula of Guha Sarkar et al. (2012) are shown in black. The solid black curve is the bias calculated using the theoretical prescription of Bagla et al. (2010) at all redshifts under consideration, and is overplotted for reference. The values of b_{HI} obtained by combining the observational results of Switzer et al. (2013) and Rao et al. (2006) at $z \sim 0.8$, the bias computed by Khandai et al. (2011) at $z \sim 0.8$ using the observations of Chang et al. (2010), and the bias value at $z \sim 0$ measured by Martin et al. (2012) for the ALFALFA sample of H I-selected galaxies are shown in colour.
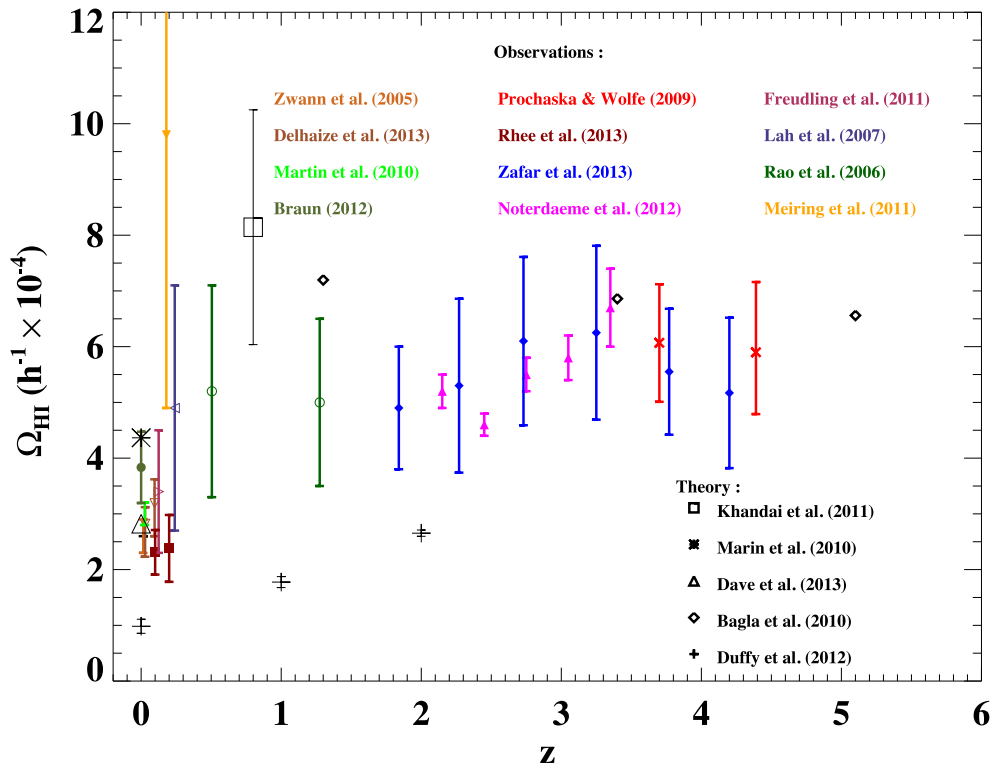

Figure 2. Compiled Ω_{HI} values in units of $h^{-1} \times 10^{-4}$ from the literature: the observations of Zwaan et al. (2005, chocolate brown solid line), Braun (2012, olive filled circle), Delhaize et al. (2013, brown open downward triangles), Martin et al. (2010, green dot), Freudling et al. (2011, maroon right triangle), Lah et al. (2007, purple left triangle), Rao et al. (2006, dark green open circles), Prochaska & Wolfe (2009, red crosses), Rhee et al. (2013, dark red filled squares), Meiring et al. (2011, orange filled downward triangle), Noterdaeme et al. (2012, magenta filled triangles), Zafar et al. (2013, blue filled diamonds), and the theoretical/simulation prescription predictions of Khandai et al. (2011), Marín et al. (2010), Davé et al. (2013), Bagla et al. (2010) and Duffy et al. (2012). The observational points are plotted in colour and the theoretical ones in black.

Switzer et al. (2013) and Rao et al. (2006) providing an estimate of b_{H_I} at $z \sim 0.8$,[11] and the value of b_{H_I} at $z \sim 0.8$ estimated by Khandai et al. (2011) using the measurement of Chang et al. (2010). The theoretical values are plotted in black and the measurements are plotted in colour.

We now use the compilation of the available measurements to obtain estimates on the values of Ω_{H_I} and b_{H_I} at intervening redshifts, as also estimates on the 1σ error bars at the intervening points. To do so, we need error estimates on all the data points for Ω_{H_I} and b_{H_I}. We use the observational points and their error bars as the data points in the case of Ω_{H_I}. The case of b_{H_I} is more speculative since there are very few observational constraints. The present constraints on b_{H_I} include

(a) the two available observations: the ALFALFA result at $z = 0$ from Martin et al. (2012), and the combination of the Switzer et al. (2013) and the Rao et al. (2006) measurement at $z = 0.8$ with the corresponding error bars.

(b) the 10 theoretical points at $z > 1$.

To obtain estimates on the uncertainties in b_{H_I}, we may consider the following three scenarios.

(a) Conservative: in this approach, we may limit the analysis to the observational uncertainties on b_{H_I}, and neglect the theoretical predictions. We, therefore, may use only the two available observations, with their error bars, to constrain the bias.

(b) Optimistic: in this alternate approach, we may consider the opposite situation, i.e. that the value of the bias is given by a theoretical model for all redshifts, with zero error. This in turn avoids the association of uncertainties to the theoretical predictions. The above two scenarios (a) and (b) are considered further in the appendix.

(c) Intermediate scenario: we consider this scenario for the remainder of the main text. To motivate the approach, we re-emphasize that the analysis for the bias is dominated by theoretical and modelling uncertainties and hence, to fully utilize the available constraints, one needs to quantify the uncertainties in the modelling at each redshift. If the scatter in individual simulations is considered as an estimate of the error, the error bars in most cases turn out to be negligibly low (corresponding effectively to case b above) and also do not reflect the range of physics input that may be used in other simulations at the same redshift. Hence, one possible method is to use the range of values of bias predicted by all the available theoretical models at a certain redshift as a measure of the range of physics uncertainties in the theoretical models. Here, we use the 10 theoretical points at $z > 1$, with a binned average to calculate the mean and 1σ deviation in four redshift bins each of width ~ 0.6 between redshifts $1 < z < 3.5$. This serves as an estimate of the error due to modelling uncertainties in the calculation of the bias factor. In this way, we obtain estimates on the mean and error bars on the bias factor at redshifts $1 < z < 3.5$. The values and error bars for Ω_{H_I} and b_{H_I} thus obtained are plotted in Fig. 4.

We note that the scenarios (b) and (c) contain contributions from the results of simulations. The choice of physics in the simulations and their possible biases, therefore, have an influence on the results obtained and their uncertainties. The validity of the results may be confirmed when further data become available at higher redshifts.

We use the algorithm for interpolation of irregularly spaced noisy data using the minimum variance estimator as described in Rybicki
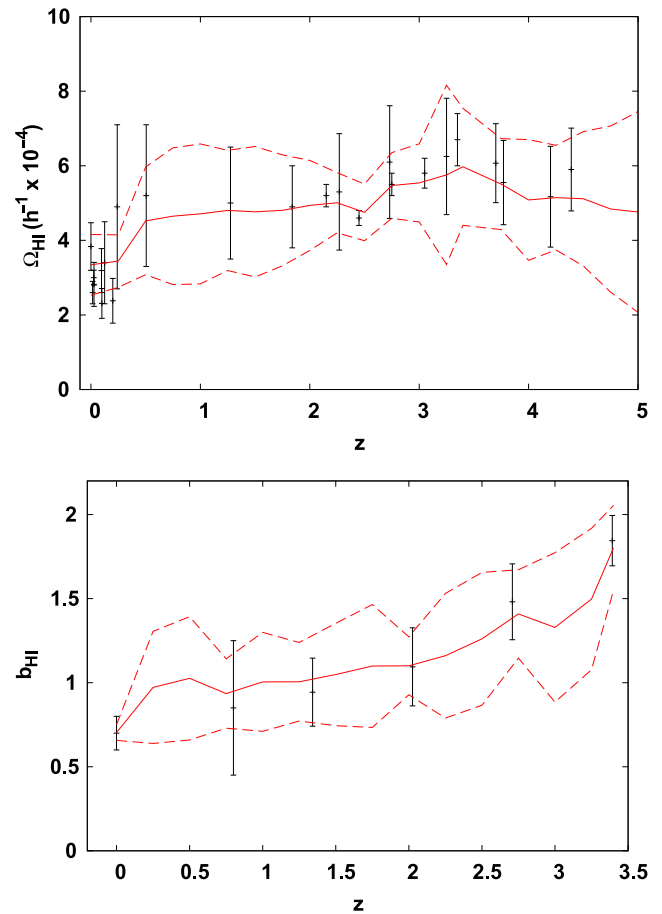

Figure 4. Compiled Ω_{H_I} values (in units of $h^{-1} \times 10^{-4}$) and b_{H_I} from the literature, with the minimum variance unbiased estimator (solid line) of Rybicki & Press (1992) overplotted along with its 1σ error in each case (dotted lines). In the case of b_{H_I}, the errors reflect the theoretical and modelling uncertainties and hence are more speculative. The bias b_{H_I} is not as accurately constrained as Ω_{H_I} from observations, however the errors at present are dominated by the range of theoretical predictions for b_{H_I} at different redshifts.

& Press (1992). This estimator is so constructed that both the error as well as the spacing between the noisy data points are taken into consideration. As an input to the algorithm, one requires an estimate of the typical (inverse) decorrelation of the sample, w, which we take to be $w = 2$ that corresponds to a decorrelation length of 0.5 (in redshift units). We also assume the value of the a priori population standard deviation $p_{sig} = 2$.[12] We implement the algorithm with the help of the fast tridiagonal solution described in Rybicki & Press (1994).[13] We thus obtain an estimate of the mean value and 1σ error bars on intervening points for both Ω_{H_I} and b_{H_I}. These are plotted as the solid and dotted lines ('snakes') of Fig. 4.

The resulting values of the mean and errors in Ω_{H_I} and b_{H_I} obtained by the interpolation of the data and the resulting estimate

---

[11] The statistical uncertainties are added in quadrature.

[12] The values of w and p_{sig} are usually well defined in the case of time series data. Increasing the value of w decreases the error on the estimate and vice versa. Similarly, increasing p_{sig} increases the error on the estimate and vice versa. We choose the values $w = 2$ and $p_{sig} = 2$, since for these values of the decorrelation length and population standard deviation, the results obtained are visually a good fit to the data points, including the error estimates.
[13] http://www.lanl.gov/DLDSTP/fast/

Table 2. Combination of the fractional uncertainty on $b_{\rm HI}$, $\Omega_{\rm HI}$ due to the currently available constraints, and the predicted resulting uncertainty (both absolute and relative) on the product $\Omega_{\rm HI}b_{\rm HI}$, which is the quantity of relevance for the calculation of the 3D temperature fluctuation power spectrum, $(\delta T_{\rm HI})^2$, at various redshifts. The range of interpolation is restricted up to redshift 3.4 due to the last bias point near $z \sim 3.4$. Note that $\Omega_{\rm HI}$ is in units of $10^{-4}\,h^{-1}$.

| z	$\Omega_{\rm HI}^a$	$\Delta\Omega_{\rm HI}^a$	$b_{\rm HI}$	$\Delta b_{\rm HI}$	$\Omega_{\rm HI}b_{\rm HI}^a$	$\Delta(\Omega_{\rm HI}b_{\rm HI})^a$	$\Delta(\Omega_{\rm HI}b_{\rm HI})/(\Omega_{\rm HI}b_{\rm HI})$
0.000	3.344	0.814	0.703	0.047	2.352	0.593	0.252
0.250	3.443	0.703	0.972	0.333	3.346	1.335	0.399
0.500	4.523	1.445	1.026	0.367	4.640	2.224	0.479
0.750	4.648	1.835	0.935	0.206	4.348	1.966	0.452
1.000	4.710	1.877	1.005	0.294	4.733	2.340	0.494
1.250	4.804	1.612	1.005	0.234	4.830	1.971	0.408
1.500	4.766	1.750	1.049	0.304	4.998	2.340	0.468
1.750	4.804	1.487	1.099	0.365	5.281	2.398	0.454
2.000	4.936	1.207	1.101	0.172	5.432	1.578	0.290
2.250	5.008	0.807	1.160	0.371	5.810	2.079	0.358
2.500	4.750	0.759	1.261	0.395	5.989	2.107	0.352
2.750	5.471	0.880	1.409	0.263	7.708	1.899	0.246
3.000	5.541	1.048	1.329	0.444	7.363	2.829	0.384
3.250	5.756	2.401	1.498	0.420	8.620	4.334	0.503
3.400	5.971	1.570	1.802	0.252	10.758	3.204	0.298

Note. ^{a}In units of $10^{-4}\,h^{-1}$.
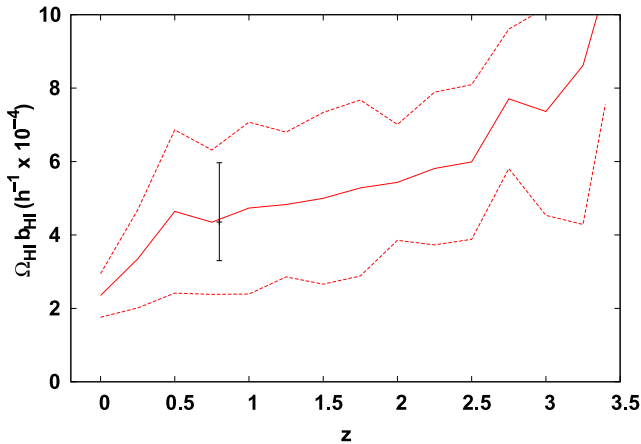
Figure 5. Compiled set of values of $\Omega_{\rm HI}b_{\rm HI}$ (in units of $h^{-1} \times 10^{-4}$), calculated using the estimates for the mean and 1σ standard deviations in $\Omega_{\rm HI}$ and $b_{\rm HI}$. The error estimate is obtained by propagating the errors in $\Omega_{\rm HI}$ and $b_{\rm HI}$. The measurement (Switzer et al. 2013) at $z = 0.8$ is also overplotted for reference.

and uncertainty in the product $\Omega_{\rm HI}b_{\rm HI}$ are listed in Table 2.[14] These are also plotted in the curves of Figs 4 and 5 along with the compiled data points and the measurement of $\Omega_{\rm HI}b_{\rm HI}$ at $z = 0.8$ (Switzer et al. 2013). These values are also fairly consistent with the uncertainties predicted by the conservative and optimistic scenarios over their ranges of applicability (see the appendix).

5 IMPACT ON THE H I POWER SPECTRUM

As can be seen from equations (1) and (2), the quantity $\Omega_{\rm HI}b_{\rm HI}$ directly appears in the expression for the H I temperature fluctuation

---

[14] The error estimates arise from a combination of (a) the magnitude of the errors on individual points as well as (b) the proximity to, and errors on, the nearby points. It can be seen that the errors at redshifts $z \sim 2.7$ are low, due to a number of nearby well-constrained points. In comparison, the errors near $z \sim 3.25$ are higher, due to the higher error bars on nearby points.

power spectrum. Therefore, the H I temperature fluctuation and its power spectrum will be uncertain by different amounts depending upon the level of variation of $\Omega_{\rm HI}$ and $b_{\rm HI}$ allowed by observational and theoretical constraints. For example, at redshifts near 1, the temperature fluctuation varies by about 50 per cent due to the variation in the product $\Omega_{\rm HI}b_{\rm HI}$ alone. However, near redshifts 2–2.75, it is more constrained and varies only by about 25–35 per cent due to the larger number of tighter constraints on $\Omega_{\rm HI}$ at these redshifts. The power spectrum $(\delta T_{\rm HI})^2$ has uncertainties of about twice this amount. Due to the very small number of data points above redshift 3.5, it is difficult to obtain constraints on $\delta T_{\rm HI}$ beyond this redshift with the presently available measurements. The $\delta T_{\rm HI}$ and its resulting uncertainty are plotted for redshifts 0, 1, 2 and 3 in Fig. 6.

The above uncertainty on the power spectrum impacts the measurements by current and future intensity mapping experiments. To provide an indication of the significance of this effect, we consider the expression for the signal-to-noise ratio (SNR) in the 21-cm signal (Feldman, Kaiser & Peacock 1994; Seo et al. 2010; Battye et al. 2012) for a single-dish radio experiment:

$$\frac{S}{N} = \sqrt{\frac{2\pi k^2 \Delta k V_{\rm sur}}{(2\pi)^3}} \frac{P_{\rm HI}}{P_{\rm HI} + (\sigma_{\rm pix}^2 V_{\rm pix}/(\bar{T}(z)^2 \hat{W}(k)^2) + P_{\rm shot}}. \tag{9}$$

In the above expression, Δk is the wavenumber range and $V_{\rm sur}$ is the survey volume. $P_{\rm HI} \equiv (\delta T_{\rm HI})^2$ is the 3D power spectrum defined in equation (1), $\bar{T}$ is the mean brightness temperature defined in equation (2) and $P_{\rm shot}$ is the shot noise. The $\sigma_{\rm pix}$ is the pixel noise defined by

$$\sigma_{\rm pix} = \frac{T_{\rm sys}}{\sqrt{t_{\rm pix}\delta\nu}}, \tag{10}$$

where $T_{\rm sys}$ is the system temperature including both the instrument and the sky temperature, $t_{\rm pix}$ is the observation time per pixel and $\delta\nu$ is the frequency interval of integration. The window function $\hat{W}(k)$ models the angular and frequency response function of the instrument. Foreground removal may be contained in a residual noise term that remains after the foreground is assumed to be subtracted.

The above SNR, thus, contains contributions from a noise term and a cosmic-variance term. If the intensity mapping experiment
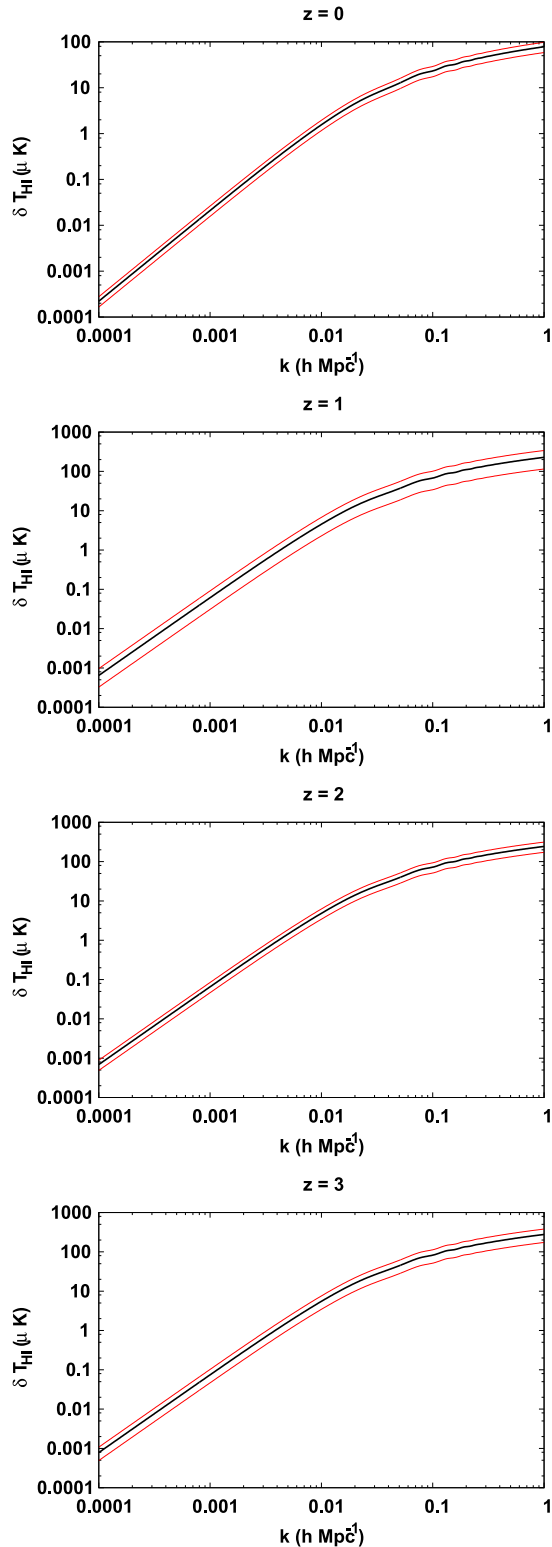
Figure 6. Impact on the H I power spectrum, $\delta T_{\mathrm{H\,I}}(k)$ due to the uncertainty in $\Omega_{\mathrm{H\,I}}$ and $b_{\mathrm{H\,I}}$ coming from the available measurements. Plots at redshifts 0, 1, 2 and 3 are shown.

is noise-dominated, the noise term $(\sigma_{\mathrm{pix}}^2 V_{\mathrm{pix}}/(\bar{T}(z)^2 \hat{W}(k)^2) + P_{\mathrm{shot}}$ dominates $P_{\mathrm{H\,I}}$. In this case, the SNR becomes proportional to the signal $P_{\mathrm{H\,I}}$. This indicates that the uncertainty in the signal translates into the uncertainty in the SNR. Hence, the observational uncertainties in the parameters $\Omega_{\mathrm{H\,I}}$ and $b_{\mathrm{H\,I}}$ have direct implications for the

range of the SNR of these experiments at different redshifts. In particular, the uncertainty of 50–100 per cent (from Table 2) in the magnitude of the power spectrum $(\delta T_{\mathrm{H\,I}})^2$, implies the corresponding uncertainty in the SNR.

At large scales, high-σ detections with upcoming telescopes like the LOFAR and the SKA may be cosmic-variance dominated (e.g. Mesinger, Ewall-Wice & Hewitt 2014). In these cases, the SNR is independent of the signal.

6 CONCLUSIONS

In this paper, we have considered recent available constraints on $\Omega_{\mathrm{H\,I}}$ and $b_{\mathrm{H\,I}}$ together with their allowed uncertainties, coming from a range of theoretical and observational sources. These are used to predict the consequent uncertainty in the H I power spectrum measured and to be measured by current and future experiments. Using a minimum variance interpolation scheme, we find that a combination of the available constraints allow a near 50–100 per cent error in the measurement of the H I signal in the redshift range $z \sim 0$–3.5. This is essential for the planning and construction of the intensity mapping experiments. Table 2 is of practical utility for quantifying the uncertainties in the various parameters. We have tested three different confidence scenarios: optimistic, conservative and an intermediate scenario, and find the predicted uncertainties in all three cases to be fairly consistent over their range of applicability. It is also clear from the analysis that a constant value of either $\Omega_{\mathrm{H\,I}}$ or of $b_{\mathrm{H\,I}}$ does not fully take into account the magnitude of the uncertainties concerned. Hence, it is important to take into account the available measurements for a more precise prediction of the impact on the H I power spectrum.

Even though we have assumed a standard Λ cold dark matter model for the purposes of this paper, the analysis may be reversed to obtain predictions for the cosmology, the evolution of the dark energy equation of state, curvature and other parameters (Chang et al. 2010; Bull et al. 2014). Again, for such purposes, a realistic estimate of the input parameters ($\Omega_{\mathrm{H\,I}}, b_{\mathrm{H\,I}}$) would be useful to accurately predict the consequent uncertainties in the parameters predicted. A model which accurately explains the value of bias at all redshifts, and the neutral hydrogen fraction is currently lacking and hence we use the present observations and theoretical prescriptions to provide the latest constraints on the 3D H I power spectrum. In the future, as better and more accurate measurements of the bias and neutral hydrogen density become available, it would significantly tighten our constraints on the power spectrum. Similarly, the clustering properties of DLAs which leads to the bias of DLAs at higher redshifts offers an estimate of the bias parameter of neutral hydrogen, though it is significantly higher.

We have indicated the implications of the predicted uncertainty in the power spectrum for the current and future intensity mapping experiments. In the case of a single-dish radio telescope, for example, the uncertainty in the power spectrum translates into an uncertainty in the SNR of the instrument in noise-dominated experiments. Thus, this has important consequences for the planning of H I intensity mapping measurements by current and future radio experiments.

REFERENCES

Ansari R. et al., 2012, A&A, 540, A129
Bagla J. S., Khandai N., Datta K. K., 2010, MNRAS, 407, 567
Barnes D. G. et al., 2001, MNRAS, 322, 486
Battye R. A. et al., 2012, preprint (arXiv:1209.1041)
Bharadwaj S., Sethi S. K., 2001, J. Astrophys. Astron., 22, 293
Bharadwaj S., Srikant P. S., 2004, J. Astrophys. Astron., 25, 67
Bharadwaj S., Nath B. B., Sethi S. K., 2001, J. Astrophys. Astron., 22, 21
Bharadwaj S., Sethi S. K., Saini T. D., 2009, Phys. Rev. D, 79, 083538
Braun R., 2012, ApJ, 749, 87
Bull P., Ferreira P. G., Patel P., Santos M. G., 2014, preprint (arXiv:1405.1452)
Catinella B. et al., 2010, MNRAS, 403, 683
Chang T.-C., Pen U.-L., Bandura K., Peterson J. B., 2010, Nature, 466, 463
Chen X., 2012, Int. J. Mod. Phys.: Conf. Ser., 12, 256
Davé R., Katz N., Oppenheimer B. D., Kollmeier J. A., Weinberg D. H., 2013, MNRAS, 434, 2645
Delhaize J., Meyer M. J., Staveley-Smith L., Boyle B. J., 2013, MNRAS, 433, 1398
Duffy A. R., Kay S. T., Battye R. A., Booth C. M., Dalla Vecchia C., Schaye J., 2012, MNRAS, 420, 2799
Eisenstein D. J., Hu W., 1998, ApJ, 496, 605
Ewen H. I., Purcell E. M., 1951, Nature, 168, 356
Feldman H. A., Kaiser N., Peacock J. A., 1994, ApJ, 426, 23
Font-Ribera A. et al., 2012, J. Cosmol. Astropart. Phys., 11, 59
Freudling W. et al., 2011, ApJ, 727, 40
Giovanelli R. et al., 2005, AJ, 130, 2598
Gong Y., Chen X., Silva M., Cooray A., Santos M. G., 2011, ApJ, 740, L20
Guha Sarkar T., Mitra S., Majumdar S., Choudhury T. R., 2012, MNRAS, 421, 3570
Jaffé Y. L., Poggianti B. M., Verheijen M. A. W., Deshev B. Z., van Gorkom J. H., 2012, ApJ, 756, L28
Johnston S. et al., 2008, Exp. Astron., 22, 151
Jonas J. L., 2009, IEEE Proc., 97, 1522
Kerp J., Winkel B., Ben Bekhti N., Flöer L., Kalberla P. M. W., 2011, Astron. Nachr., 332, 637
Khandai N., Sethi S. K., Di Matteo T., Croft R. A. C., Springel V., Jana A., Gardner J. P., 2011, MNRAS, 415, 2580
Komatsu E. et al., 2009, ApJS, 180, 330
Lah P. et al., 2007, MNRAS, 376, 1357
Lah P. et al., 2009, MNRAS, 399, 1447
Lang R. H. et al., 2003, MNRAS, 342, 738
Lanzetta K. M., Wolfe A. M., Turnshek D. A., Lu L., McMahon R. G., Hazard C., 1991, ApJS, 77, 1
Linder E. V., Jenkins A., 2003, MNRAS, 346, 573
Marín F. A., Gnedin N. Y., Seo H.-J., Vallinotto A., 2010, ApJ, 718, 972
Martin A. M., Papastergis E., Giovanelli R., Haynes M. P., Springob C. M., Stierwalt S., 2010, ApJ, 723, 1359
Martin A. M., Giovanelli R., Haynes M. P., Guzzo L., 2012, ApJ, 750, 38
Masui K. W. et al., 2013, ApJ, 763, L20
Meiring J. D. et al., 2011, ApJ, 732, 35
Mesinger A., Ewall-Wice A., Hewitt J., 2014, MNRAS, 439, 3262
Meyer M. J. et al., 2004, MNRAS, 350, 1195
Muller C. A., Oort J. H., 1951, Nature, 168, 357
Noterdaeme P., Petitjean P., Ledoux C., Srianand R., 2009, A&A, 505, 1087
Noterdaeme P. et al., 2012, A&A, 547, L1
Obreschkow D., Klöckner H.-R., Heywood I., Levrier F., Rawlings S., 2009, ApJ, 703, 1890

Oosterloo T., Verheijen M., van Cappellen W., 2010, Proc. Sci. 043 (International SKA Forum 2010), Assen, The Netherlands, ASTRON Netherlands
Planck Collaboration XVI 2014, A&A, 571, A16
Pober J. C. et al., 2013, AJ, 145, 65
Prochaska J. X., Wolfe A. M., 2009, ApJ, 696, 1543
Rahmati A., Pawlik A. H., Raicevic M., Schaye J., 2013, MNRAS, 430, 2427
Rao S. M., Turnshek D. A., Nestor D. B., 2006, ApJ, 636, 610
Rhee J., Zwaan M. A., Briggs F. H., Chengalur J. N., Lah P., Oosterloo T., Hulst T. v. d., 2013, MNRAS, 435, 2693
Rybicki G. B., Press W. H., 1992, ApJ, 398, 169
Rybicki G. B., Press W. H., 1994, Contrib. Mineral. Petrol., p. 5004
Saiyad Ali S., Bharadwaj S., 2014, J. Astrophys. Astron., 35, 157
Scoccimarro R., Sheth R. K., Hui L., Jain B., 2001, ApJ, 546, 20
Seo H.-J., Dodelson S., Marriner J., Mcginnis D., Stebbins A., Stoughton C., Vallinotto A., 2010, ApJ, 721, 164
Sheth R. K., Tormen G., 2002, MNRAS, 329, 61
Springel V. et al., 2005, Nature, 435, 629
Swarup G., Ananthakrishnan S., Kapahi V. K., Rao A. P., Subrahmanya C. R., Kulkarni V. K., 1991, Curr. Sci., 60, 95
Switzer E. R. et al., 2013, MNRAS, 434, L46
Villaescusa-Navarro F., Viel M., Datta K. K., Choudhury T. R., 2014, J. Cosmol. Astropart. Phys., 09, 050
Wang L., Steinhardt P. J., 1998, ApJ, 508, 483
Wyithe J. S. B., 2008, MNRAS, 388, 1889
Wyithe J. S. B., Brown M. J. I., 2010, MNRAS, 404, 876
Wyithe J. S. B., Loeb A., 2008, MNRAS, 383, 606
Wyithe J. S. B., Loeb A., 2009, MNRAS, 397, 1926
Wyithe J. S. B., Loeb A., Geil P. M., 2008, MNRAS, 383, 1195
Zafar T., Péroux C., Popping A., Milliard B., Deharveng J.-M., Frank S., 2013, A&A, 556, A141
Zwaan M. A., Meyer M. J., Staveley-Smith L., Webster R. L., 2005, MNRAS, 359, L30

APPENDIX A: CONSERVATIVE AND OPTIMISTIC ESTIMATES ON THE UNCERTAINTIES IN THE H I POWER SPECTRUM

In this appendix, we consider the two additional possible scenarios of modelling the uncertainties on the bias parameter $b_{\mathrm{H\,I}}$, which were denoted by cases (a) and (b) in Section 4 of the main text.

(a) Conservative: this approach has the justification that it utilizes all the available observations and their associated error bars, and avoids any ambiguity related with assigning errors to simulation data. However, since the observations are limited to $z \lesssim 1$, the minimum variance estimator is also limited to this redshift range, with associated uncertainties that use only the two available $b_{\mathrm{H\,I}}$ measurements at $z \lesssim 1$. This is plotted in Fig. A1 along with the estimate for the product $\Omega_{\mathrm{H\,I}} b_{\mathrm{H\,I}}$, and the table of predicted uncertainties is provided in Table A1. Over the relevant redshift range $z \lesssim 1$, the constraints are fairly similar to those in the intermediate scenario (considered in the main text). Since we only have two observational data points over this redshift range, the mean values and uncertainties depend only upon these two observational measurements. Hence, the constraints on the bias $b_{\mathrm{H\,I}}$ are also expected to be of the same order as those in the intermediate scenario, over this redshift range. However, we cannot predict uncertainties in the bias and the power spectrum for redshifts $z > 1$ due to the unavailability of observational data, and hence this scenario may be termed conservative.

(b) Optimistic: motivation for this approach comes from providing a strict lower limit to the uncertainties in the H I signal, using the
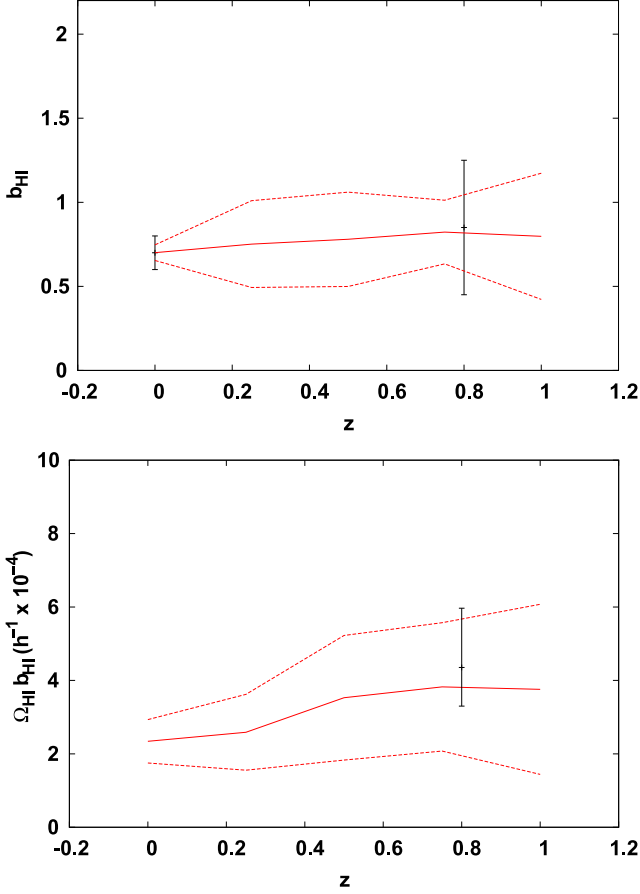
Figure A2. Optimistic estimates for the product $\Omega_{H_I}b_{H_I}$, taking into account the available observations for the uncertainties in Ω_{H_I} and neglecting uncertainties in b_{H_I} associated with theory/simulations. The measurement (Switzer et al. 2013) at $z = 0.8$ is also overplotted for reference.

Table A2. Same as Table 2 for the 'optimistic' case, where only uncertainties in Ω_{H_I} are considered, assuming that $\Delta b_{H_I} = 0$ for all redshifts. The final column provides strict lower limits on the relative uncertainty in the amplitude of the H I signal. Note that Ω_{H_I} is in units of $10^{-4}\, h^{-1}$.

z	$\Omega_{H_I}^a$	$\Delta\Omega_{H_I}^a$	b_{H_I}	$\Omega_{H_I}b_{H_I}^a$	$\Delta(\Omega_{H_I}b_{H_I})^a$	$\Delta(\Omega_{H_I}b_{H_I})/$ $(\Omega_{H_I}b_{H_I})$
0.000	3.344	0.814	0.812	2.715	0.661	0.243
0.250	3.443	0.703	0.843	2.903	0.592	0.204
0.500	4.523	1.445	0.880	3.978	1.271	0.319
0.750	4.648	1.835	0.925	4.301	1.698	0.395
1.000	4.710	1.877	0.980	4.616	1.839	0.398
1.250	4.804	1.612	1.040	4.995	1.676	0.336
1.500	4.766	1.750	1.106	5.273	1.936	0.367
1.750	4.804	1.487	1.177	5.654	1.750	0.310
2.000	4.936	1.207	1.253	6.184	1.512	0.245
2.250	5.008	0.807	1.332	6.669	1.075	0.161
2.500	4.750	0.759	1.415	6.722	1.074	0.160
2.750	5.471	0.880	1.501	8.213	1.321	0.161
3.000	5.541	1.048	1.591	8.814	1.668	0.189
3.250	5.756	2.401	1.683	9.689	4.042	0.417
3.400	5.971	1.570	1.739	10.386	2.730	0.263

Note. ^{a}In units of $10^{-4}\, h^{-1}$.

shows the resulting uncertainty on the product $\Omega_{H_I}b_{H_I}$, and Table A2 tabulates the uncertainties. We note that this scenario, while being optimistic, (a) uses both the theoretical (for the mean value) and observational (for the error bars) constraints on the parameters b_{H_I} and Ω_{H_I} respectively, and, (b) importantly, recovers a lower limit on the predicted H I uncertainty.

Figure A1. Conservative estimates for b_{H_I} and the product $\Omega_{H_I}b_{H_I}$, taking into account the available observations only, without any theoretical predictions. The measurement (Switzer et al. 2013) at $z = 0.8$ is overplotted on the product curve for reference.

Table A1. Same as Table 2 for the 'conservative' case where only observational uncertainties contribute to b_{H_I}. Note that Ω_{H_I} is in units of $10^{-4}\, h^{-1}$.

z	$\Omega_{H_I}^a$	$\Delta\Omega_{H_I}^a$	b_{H_I}	Δb_{H_I}	$\Omega_{H_I}b_{H_I}^a$	$\Delta(\Omega_{H_I}b_{H_I})^a$	$\Delta(\Omega_{H_I}b_{H_I})/$ $(\Omega_{H_I}b_{H_I})$
0.000	3.344	0.814	0.700	0.046	2.342	0.591	0.252
0.250	3.443	0.703	0.751	0.258	2.587	1.033	0.399
0.500	4.523	1.445	0.780	0.280	3.527	1.696	0.481
0.750	4.648	1.835	0.823	0.189	3.825	1.748	0.457
1.000	4.710	1.877	0.798	0.376	3.757	2.317	0.617

Note. ^{a}In units of $10^{-4}\, h^{-1}$.

uncertainties in Ω_{H_I} alone. Here, we consider a theoretical model[15] which predicts the value of b_{H_I} at all redshifts (Bagla et al. 2010). We combine the predictions of the bias from the model, assuming negligible errors, with the observational constraints on Ω_{H_I}. Fig. A2

---

[15] We emphasize that the model under consideration is only for illustrative purposes, since our aim is to quantify the uncertainty in the H I signal rather than to forecast the magnitude of the signal.
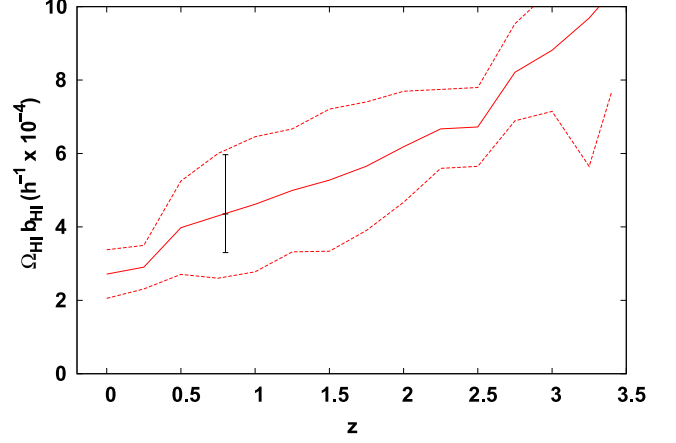
This paper has been typeset from a TeX/LaTeX file prepared by the author.